# A numerical study of a cold-mode fluidized bed reactor designed for pyrolysis of plastics

Feichi Zhang[1,*], Salar Tavakkol[1], Stefan Dercho[1], Lukas Bohlender[1], Thorsten Zirwes[2], Michael Zeller[1], Jonas Vogt[1], Dieter Stapf [1]

* feichi.zhang@kit.edu

[1]*Institute for Technical Chemistry, Karlsruhe Institute of Technology (KIT), Herrmann-von-Helmholtz-Platz 1, 76344 Eggenstein-Leopoldshafen*
[2]*Institute for Combustion Technology, University of Stuttgart, Pfaffenwaldring 31, 70569 Stuttgart*

**Abstract**

Numerical simulations have been conducted for a cylindrical, laboratory-scale fluidized bed reactor, which has been designed for fundamental research of plastic pyrolysis. The Euler-Lagrange multiphase particle-in-cell (MP-PIC) approach has been used for modeling the dense particle-load flow. As the performance of the fluidized bed heavily relies on the interaction between gas and particles, the cold flow model considering only inert quartz sand particles as bed material and nitrogen as fluidizing agent at atmospheric condition has been applied in this work. The objective of this work is to study the hydrodynamic behaviors of the fluidized bed, which is of significant importance for an efficient mixing between the bed materials in terms of heat and mass transfer.

In accordance with the experiment, the simulations have shown the bubbling fluidization regime in most considered cases, showing intermittently rising bubbles from the ground of the reactor to the upper surface of the fluidized bed. The calculated pressure drop $\Delta p$ yields a good agreement with measured data, which remains constant with varied superficial gas velocity $u_G$ and increases with the bed inventory $m_S$. The bed height $h_B$ increases slightly with increased $u_G$ due to the formation of larger bubbles. In addition, $h_B$ increases almost proportionally with $m_S$ due to the higher amount of sand mass.

While up-scaling the reactor at constant $\Delta p$ and $u_G$, the fluidized bed is dominated by large-scale bubbles for relatively small reactor diameters at $d_R$ = 3 cm and 5 cm, where the bubbles have a similar size compared with $d_R$. However, multiple-column bubbles rising along off-centered axes have been detected for further up-scaled reactor with $d_R$ = 10 cm. In this case, the parallelly rising large-scale bubbles results in a recirculation of the gas flow and accumulation of the sand particles along the centerline axis, leading to an improved mixing. In summary, the simulations are able to reproduce the behavior of the fluidized bed observed in the experiments, which confirms the validity of the used computational approach. The correlations between the operational characteristics and the operating parameters obtained from the simulations can be used for further optimized design of the fluidized bed, e.g., concerning scale-up of the reactor.

## Introduction

The global plastic production has expanded rapidly over the last years due to the vast application areas of plastics, e.g., in packaging, engineering, construction, medical sectors, which has increased 20-fold over the past 70 years, from 2 Mt in 1950 to 390.7 Mt in 2021 [1, 2]. This has led to an increasing accumulation of waste plastics in our environment. Until 2015, about 6300 Mt plastics waste has been generated [3]. Meanwhile, the traditional treatments of plastic wastes, i.e., landfilling and incineration, are used for about 75% of total plastic wastes globally in 2016, which results in serious pollutant problems like contamination of ground or ocean water, and emission of greenhouse gases [4]. In

contrast, only 12% of the plastic wastes have been recycled [4], mainly via mechanical recycling, which represents a down-cycling process and cannot be repeated infinitely [5]. In addition, the mechanical recycling of plastic wastes requires a high grade of purity of fed plastic waste to ensure the quality of regenerated plastic materials, which limits its application.

To increase circularity of plastics, chemical recycling via pyrolysis has been regarded as a promising technology in recent years, according to its advantages in handling mixed and contaminated plastics [6]. During the pyrolysis process, plastic polymers are degraded at high temperature condition to a wide range of short-chain hydrocarbons. Depending on the polymer used and the process parameters, mainly waxy products, oils, gases or monomers can be recovered as products [7, 8]. The pyrolysis oil can be reused in crackers or refineries for creating basic building blocks, such as circular ethylene and other circular by-products, which can be used for the production of new plastic products [9].

Different techniques have been used to study the pyrolysis process of plastics in recent years, among them, the thermogravimetry, the autoclave, the tubular or the screw reactor [10]. In addition to these methods, an indirectly heated fluidized bed has been applied by Kaminsky et al. [11, 12] for the recovery of mixed plastics via pyrolysis. In fact, fluidized beds are widely used in chemical and process industries for thermal treatment of granular materials via combustion or gasification [13]. The main advantages of performing pyrolysis in fluidized beds are given by the excellent heat and mass transfer as well as the capability of a continuous operation mode. In an optimal fluidized bed reactor, the rate of heat transfer can be ten times larger than in a melting vessel or tubular reactor [12]. By reducing the residence time by means of enhanced heat transfer, the polymer degrades under fast pyrolysis condition, thereby reducing unwanted side reactions and by-products [14]. To enable an efficient implementation of the fluidized bed technique for plastic pyrolysis and to optimize the operating conditions towards establishing industry-scale pyrolysis plants for waste plastics, detailed knowledge of the underlying thermochemical processes as well as the complex interplay between the fluid dynamics, heat transfer, and chemical reaction is required. In particular, the mixing behaviour of granular particles in fluidized bed represents an essential aspect for the operating performance and product yields.

Overall objective of the work is therefore to explore fluidized bed as an enabling technology for industrial-scale plastic pyrolysis, which has the potential to become a commercialized technology and solve the pollution problem caused by waste plastics. For that purpose, a laboratory-scale fluidized bed has been designed and experimentally studied at the Institute for Technical Chemistry (ITC) at the Karlsruhe Institute of Technology (KIT). As experimental studies are limited by optical access and other conditions such as time, costs and space requirements, highly-resolved numerical simulations have been conducted in this work to gain an in-depth understanding of the underlying chemo-physical processes.

The performance of fluidized beds depend strongly on the hydrodynamic behavior of the bed materials and their interactions with the gas bubbles within the reactor. Therefore, the cold flow model has been widely applied to study the effects of operating parameters on the fundamental characteristics of the fluidized bed such as bubble morphology or pressure drop. Following this idea, the simulations have been carried out under isothermal conditions and considering only inert sand particles as bed material. Focus of the work is to validate the model with respect to the hydrodynamic behaviors of the fluidized bed. For that purpose, a suitable numerical setup is established, which can reproduce the hydrodynamic behavior of the considered fluidized beds with reliable accuracy and at moderate computational cost. Thereafter, a systematical study on the correlations of the operating behaviors of the considered fluidized bed with the general operating parameters has been conducted, which allows an assessment of optimal process conditions in terms of mixing performance. The simulation results provide a detailed insight into the hydrodynamic behaviors of the fluidized bed at different operating conditions, which is of significant importance for further optimization and intensification of the pyrolysis process of plastics via fluidized bed.

## Simulation setups

- **Simulation methods**

As a detailed resolution of the gas-solid interface is computationally too expensive [15], this work applies a hybrid Euler-Lagrange approach for modelling the multiphase momentum transfer in the fluidized bed with dense particle concentration. In this case, a number of Lagrange parcels, which represent collections of spherical sand particles with predefined velocity and size, are introduced from

given locations into the computational domain and tracked during the simulations. A computationally improved model called the Multiphase Particle in Cell (MP-PIC) method developed by Andrews and O'Rourke [16] has been used to account for the inter-particular interactions. In contrast to the Discrete Element Method (DEM) or the Discrete Particle Method (DPM), where each particle-particle impact is tracked individually, the MP-PIC model evaluates the inter-particle forces by utilizing the kinetic theory of granular flows [17]. In this method, the collision forces between the particles are calculated by means of a particle pressure tensor, which is evaluated based on the local volume fraction of particles. The higher is the volume fraction of solid phase, the larger is the resulting collisional force between the particles. The scattering of particles due to the off-center collisions is modeled with a deterministic-stochastic isotropy model, which calculates the probability of collisions for each pair of parcels in the cell volume. The states of the two colliding parcels are then corrected by means of an updated velocity based on the outcome of the collision [18, 19]. The rebound model has been applied for the particle-wall collisions, where the impinging solid particles are bounced back against the wall. The simulations have been performed in an incompressible framework, assuming isothermal conditions and a constant gas density.

- **Experimental conditions**

The laboratory-scale fluidized bed reactor has a cylindrical geometry with a diameter of 5 cm and a length of 100 cm. A porous sintered metal plate is used at the ground of the reactor as gas distributor, which is only permeable to the gas and generates homogeneous regular incoming gas flow towards the bed materials. Quasi-spherical silica sand particles with a Gaussian size distribution and an arithmetic mean diameter of 212 µm have been used as carrier material (see Fig.2 too), along with nitrogen as fluidizing agent. Figure 1 on the left shows the experimental test rig along with a snapshot of the fluidized bed in cold-mode condition. The bulk gas flow velocity $u_g$ has been varied from 13.6 cm/s to 29.7 cm/s and the bed inventory $m_s$ from 195 g to 586 g, as shown in the in the middle part of Fig.1. These conditions have been selected according to the design of the fluidized bed reactor that leads to a bubbling fluidization regime, giving the best mixing behaviour of the bed material. The experiments have been conducted at atmospheric condition at 25 °C and 1 atm. Video records have been taken to assess the fluidization behaviour of the sand bed and the pressure drop has been determined based on measurement of static pressure of the gas phase at different locations within the reactor.

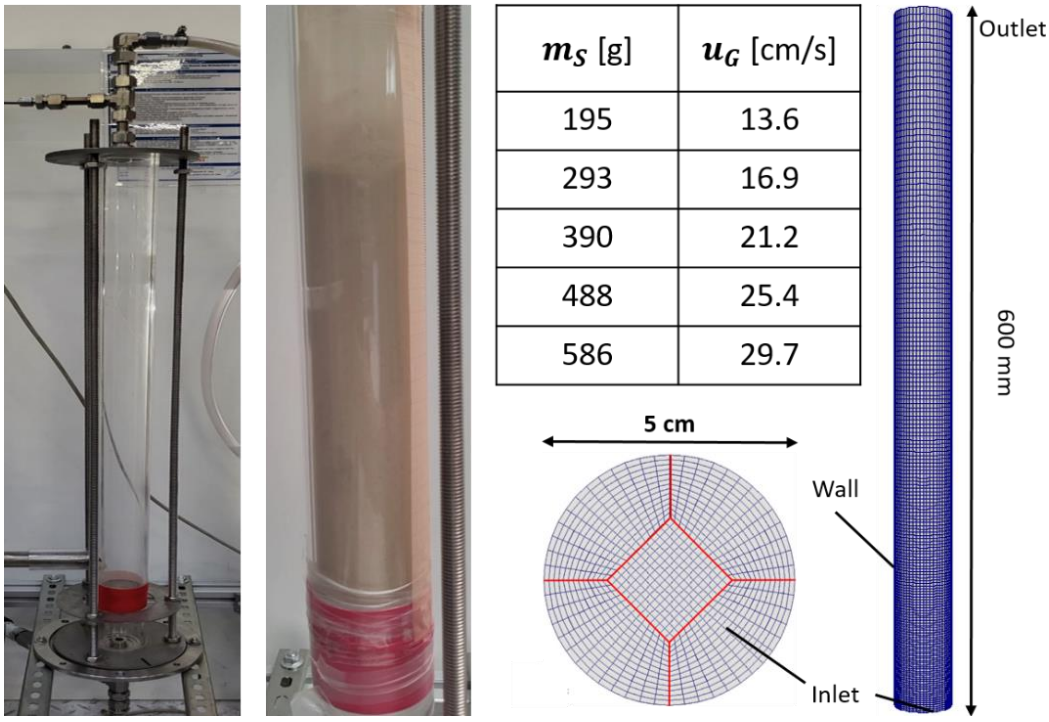


**Figure 1:** Test rig used for experimental study of a laboratory-scale fluidized bed (left) and topology of the computational grid used for the numerical simulations of the considered fluidized bed (right). The operating parameters with superficial gas velocity and total sand mass are given in the middle.

- **Computational grid**

The computational domain has been built up by a cylindrical tube, which has a length of 60 cm and a diameter as the one used in the experiment. As shown in Fig.1 in the middle lower part, the topology of the computational grid for the cross-sectional area is given by an O-type grid, which creates uniformly distributed grid cells from the centre to the wall boundaries with an almost equidistant grid length of 1.2 mm in the radial direction. The grid resolution in the longitudinal direction is 1 mm at the ground of the tube, which increases with a small expansion factor in the axial distance, as shown on the right of Fig.1. Overall, the length of the cylindrical domain has been resolved with 180 cells and the diameter of the tube with more than 30 cells, which leads to approx. 150,000 hexahedral elements in total.

- **Boundary conditions**

The boundaries of the gas domain are indicated in Fig.1 on the right, where nitrogen gas enters the domain from the inlet and leaves the domain at the outlet. A non-slip condition is used for the reactor wall. The flow velocity at the inlet is calculated from $u_{G,Inlet} = u_{G,0}/\varepsilon$, with the bulk flow velocity of the gas $u_{G,0}$ and the void fraction or porosity $\varepsilon$. In case of $\varepsilon = 1$ or without sand particles, the inlet flow velocity is equal to the superficial gas flow velocity ($u_{G,Inlet} = u_{G,0}$); if sand particles are available or $\varepsilon \neq 1$, the inlet flow is larger than $u_{G,0}$ to preserve continuity. The pressure at the outlet is fixed at ambient pressure, whereas its gradient at the reactor wall and at the inlet is set to zero. The simulations have been conducted under isothermal condition at 25 °C and 1 atm. The densities of the gas and the sand are $\rho_G$ = 1.14 kg/m$^3$ and $\rho_S$ = 2660 kg/m$^3$.

Four million Lagrange parcels have been used to model the dynamics of the sand particles for all cases. Therefore, the number of particles per parcel increases with increased bed inventory or amount of sand, respectively. The Gauss-normal distribution with a mean value of 213 µm and a standard deviation of 72 µm has been used to reproduce the measured size distribution of sand particles in the fluidized bed. As shown in Fig.2, the measured and calculated probability density functions (PDF) of the particle diameter show a reasonably good agreement. The deviations between both PDFs from experiment and simulation are attributed to the asymmetric distribution of the measured PDF of particle size. The particles are initialized uniformly in space along the whole domain, which fall down onto the ground of the reactor by gravitational force and interact with the incoming gas flow, forming a fluidized sand bed.

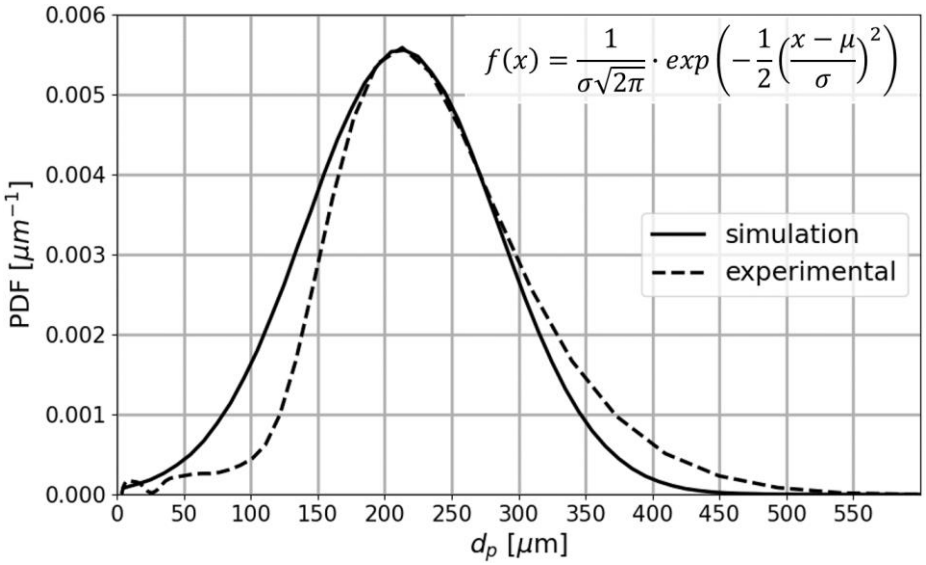


**Figure 2:** Comparison of particle size distributions used for the experiments and simulations.

- **Modeling concept**

The open-source code OpenFOAM-v2112 [20] has been used to perform the numerical simulations and the standard solver "MPPICFoam" available in OpenFOAM has been applied in the current work to simulate the gas-solid flow in the fluidized bed. The balance equations have been solved in an

incompressible formulation, employing a 1st order interpolationscheme (upwind) for discretization of the convection and a 2nd order scheme for the diffusion term. The time step is set to 0.1 ms, ensuring a maximum CFL (Courant-Friedrichs-Lewy) number at approx. unity. The simulations have been run for a physical time of 8 s with 128 CPU cores (1 node) from the HAWK cluster at the high performance computing center Stuttgart (HLRS). One second after the initialization of the fluidized bed simulation, statistical averaging of the flow has been performed for a physical time of 7 s, corresponding to more than 5 flow-through times based on the superficial gas velocity and the bed height.

**Simulation Results**

- **Fluidization morphology**

Figure 3 illustrates instantaneous contours of the void fraction or porosity $\varepsilon$ on a meridian cutting plane passing through the centerline axis, on the left for increasing superficial gas velocity from $u_G$ = 14 to 30 cm/s and on the right for increasing bed inventory from $m_S$ = 195 g to 586 g. The black points indicate a small portion (ca. 1%) of the totally tracked 4 million Lagrangian parcels for representation of the sand particles, which are up-scaled by a factor of 5 for better visualization. The bubbles can be identified by the regions with large $\varepsilon$ within the reactor. The case with the smallest $u_G$ at 14 cm/s reveals a smooth or close-to-minimum fluidization regime, where the sand bed yields a weak fluidization, without showing clear bubble formation. A further increase of $u_G$ to 17, 21 and 25 cm/s results in formation of a number of bubbles, corresponding to the bubbling fluidization regime. These bubbles rise along the axial direction due to buoyancy, which burst at the upper boundary of the fluidized bed. The size of the generated bubbles increases with $u_G$, and the hydrodynamics of the fluidized bed at the highest velocity with $u_G$ = 30 cm/s is dominated by large bubbles even with a size close to the reactor diameter. This behavior is closely related to the slugging fluidization regime. The enhanced bubble formation at increased $u_G$ is attributed to the increased momentum flux of the gas flow, leading to a reinforced gas-to-solid momentum transfer and recirculation of the sand particles towards the reactor wall.

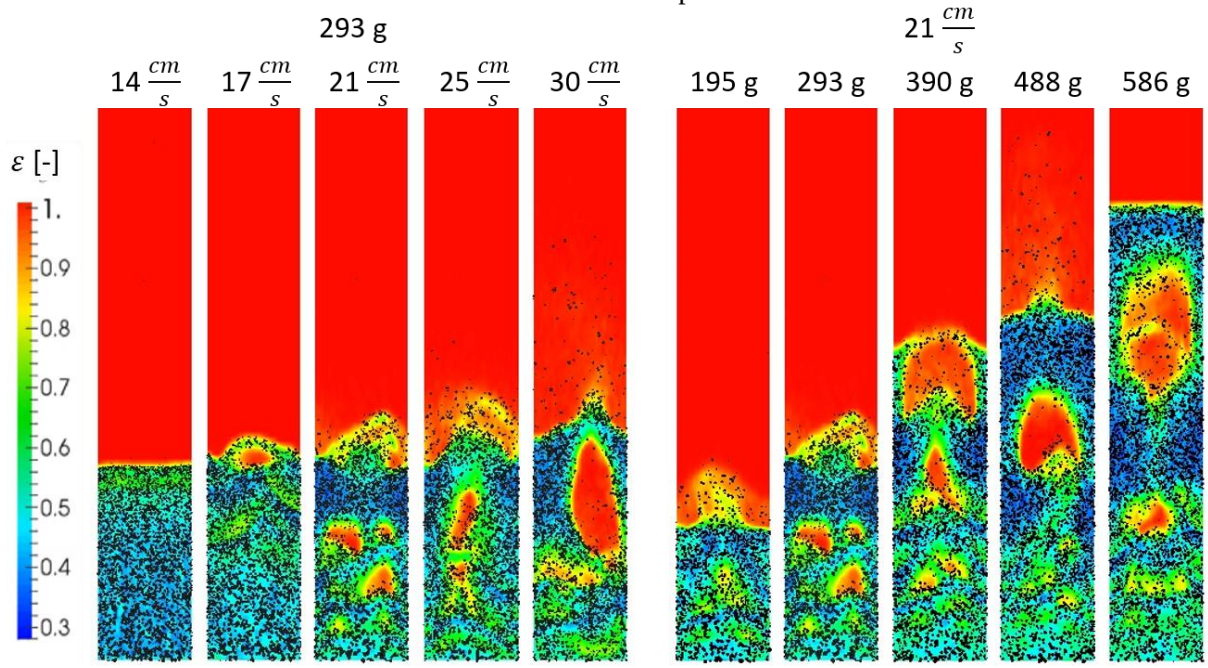


**Figure 3:** Instantaneous contours of void fraction on a cutting plane passing through the centerline axis calculated from MP-PIC simulations of a laboratory-scale fluidized bed: on the left for increasing superficial gas flow velocity and on the right for increasing bed inventory.

In the bubbling fluidization regime, the sand particles are driven to the reactor walls by the rising bubbles, leading to a core-annulus flow pattern where the gas phase dominates along the centerline axis and sand particles are located near the walls. As the gas flow velocity is low or close to zero at the wall due to the non-slip condition, the particles fall down along the wall to a region close to the base of the reactor and interact with the incoming gas and the small-scale bubbles at a higher velocity. The sand particles are then pushed back towards the upper surface of the reactor together with the rising bubbles,

leading to a circular motion of the sand particles. In the cases of large $u_G$, the sand particles are even ejected upwards to the outside of the upper surface of the fluidized bed during bursting of the bubbles, as illustrated for the cases with $u_G$ = 25 cm/s and 30 cm/s on the left of Fig.3.

While increasing $m_S$at constant $u_G$ = 21 cm/s, as shown in Fig.3 on the right, the morphology of the bubbling fluidized bed remains almost unchanged. However, the height of the sand bed $h_B$ increases significantly with $m_S$, which is attributed to the increased amount of sand particles. As $h_B$ increases with $m_S$, the small bubbles generated near the ground of the reactor have more space to develop and to coalesce with each other, so that the size of the bubbles increases with $m_S$. The morphological behavior obtained from the simulations agrees well with the experimental observations and reproduces the expected fluidization regimes based on the preliminary design of the considered fluidized bed. The desired bubbling fluidization regime can be achieved for a moderate range of $u_G$ and $m_S$, which is beneficial with regard to an efficient mixing and heat-/mass transfer.

- **Pressure drop and bed height**

While passing through the sand bed, the gas flow yields a pressure loss $\Delta p$ due to exchange of momentum or kinetic energy between the gas and the solid phases. In the fixed bed regime, $\Delta p$ increases linearly with $u_G$ [21]. In the case of that $u_G$ is larger than the minimum fluidization velocity, the solid particles are carried by the gas flow and attain as a whole a fluid-like behaviour. The weight of the particles is balanced by the drag force exerted by the fluid flow on the particles, which results in a pressure loss of the gas phase [21]

$$\Delta p = \frac{F_g - F_A}{A_0} = \frac{V_S \cdot (\rho_S - \rho_G) \cdot g}{A_0} = h_B \cdot (1 - \varepsilon) \cdot (\rho_S - \rho_G) \cdot g \qquad (1)$$

where $F_g$ and $F_A$ are the gravitational and buoyancy force, $A_0$ and $V_S$ are the cross-sectional area and the volume of all sand particles. Figure 4 on the left compares the measured and calculated $\Delta p$, which show a reasonably good agreement. $\Delta p$ remains almost constant with increased $u_G$. The reason is attributed to the fact that $\Delta p$ is equivalent with the overall particle weight per unit bed cross-sectional area, as shown in Eq.(1). Therefore, $\Delta p$ is not influenced by $u_G$. In contrast, $\Delta p$ increases with $m_S$ due to the increased $h_B$ or total mass of sand, respectively, which is in accordance with Eq.(1). The simulations have reproduced correctly the correlations of $\Delta p$ with respect to $u_G$ and $m_S$.

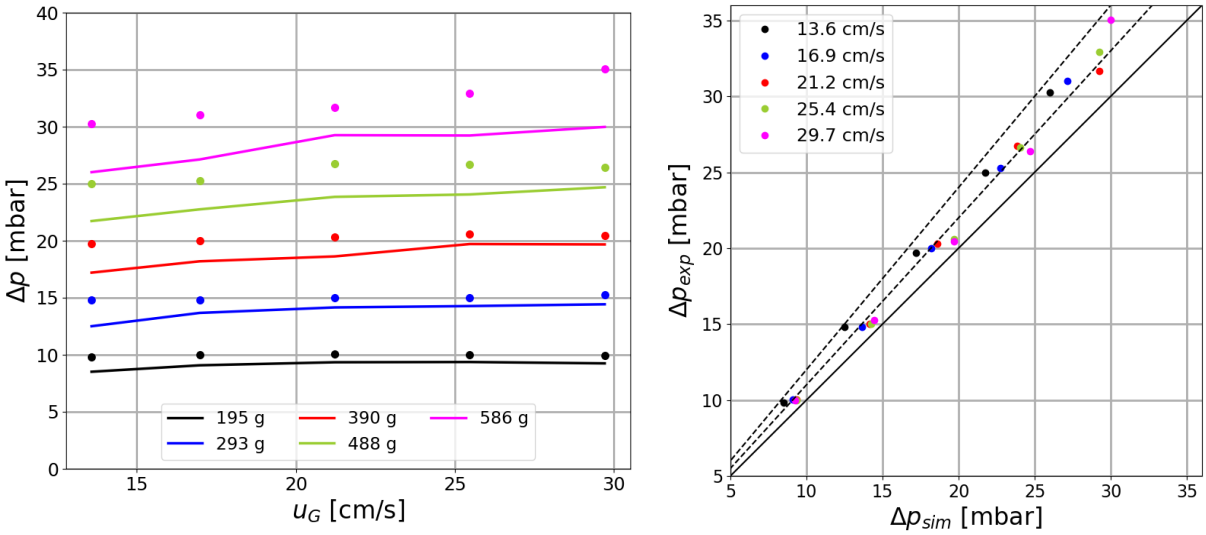


**Figure 4:** Comparison of measured and calculated pressure drop under different operating conditions (left); measured vs. calculated pressure drop for illustration of the deviation between them (right).

However, $\Delta p$ from the simulations is underestimated compared with the measurement. The reason could be attributed the assumptions used in the simulations, which leads to prediction of a lower energy loss in the system. For instance, the gas is assumed to be incompressible and the particles are assumed to have ideal spherical shape. In addition, the frictional energy loss caused by particle-particle/-wall collisions has not been modeled in a detailed way and the angular momentum of the sand particles is not considered by the current MP-PIC approach. As a result, the energy loss during momentum or energy

exchange between the gas and the solid phase is underestimated. The difference between $\Delta p_{Exp}$ and $\Delta p_{Sim}$ increases with $m_S$, as these effects become more pronounced with increased $m_S$.

In order to illustrate the differences between the experiments and the simulations in detail, Fig.4 on the right plots the measured $\Delta p$ against the calculated $\Delta p$, i.e., $\Delta p_{Exp}$ vs. $\Delta p_{Sim}$, where envelope curves with $\Delta p_{Exp} = \Delta p_{Sim}$ (solid line), $\Delta p_{Exp} = 1.1\Delta p_{Sim}$ and $\Delta p_{Exp} = 1.2\Delta p_{Sim}$ (dashed lines) are used to identify the ratios of $\Delta p_{Exp}/\Delta p_{Sim}$. As shown in Fig.4 on the right, all data pairs with $\Delta p_{Exp}$ vs. $\Delta p_{Sim}$ are below the reference line of $\Delta p_{Exp} = 1.2\Delta p_{Sim}$, indicating that the deviation between measured and calculated $\Delta p$ is less than 20% for all cases. Despite the discrepancies between experiments and simulations, the hydrodynamic behaviors with regard to fluidization behavior of the considered fluidized bed has been reproduced in a qualitatively or even quantitatively correct way, which validates the numerical approach used in this work.

Figure 5 on the left depicts profiles of time-averaged particle volume fraction $\bar{\alpha}_P$ along the centerline axis, on the left for a constant $m_S$ at 390 g with varied $u_G$ and in the middle for the reference $u_G$ at 21 cm/s with varied $m_S$. The right-hand side of Fig.5 shows time-mean contours of $\bar{\alpha}_P$ on a cutting plane across the symmetry axis for the reference case with $u_G$ = 21 cm/s and $m_S$ = 390 g. At $u_G$>13.6 cm/s, where the fluidized bed is characterized by the bubbling fluidization regime, $\bar{\alpha}_P$ is at largest at the ground surface of the reactor with a maximum value of $\bar{\alpha}_P \approx 0.5$, and it decreases to 0 at the upper surface of the sand bed. In the case with $u_G$=13.6 cm/s, the fluidized bed is subjected to the close-to-minimum fluidization regime, without clear formation of bubbles, as shown in Fig.3 on the left. Therefore, the maximum of $\bar{\alpha}_P$ is located in an intermediate range between the ground and upper surface of the reactor. With further increased superficial gas velocity, the sand particles are pushed more strongly away from the centerline due to the increased momentum flux of the gas flow, so that $\bar{\alpha}_P$ decreases with increased $u_G$. As indicated in Fig.5 on the right, $\bar{\alpha}_P$ increases in the radial direction from the centerline and reaches its maximum in a region near to the reactor wall. In addition, it can be detected from the profiles of $\bar{\alpha}_P$ in Fig.5, that $\bar{\alpha}_P$ decreases faster with increased $u_G$ and $m_S$, indicating a decrease of the bed height $h_B$ with $u_G$ and $m_S$. However, the effect of $u_G$ on $h_B$ is subordinate compared with the impact of $m_S$ on $h_B$, as illustrated in Fig.3.

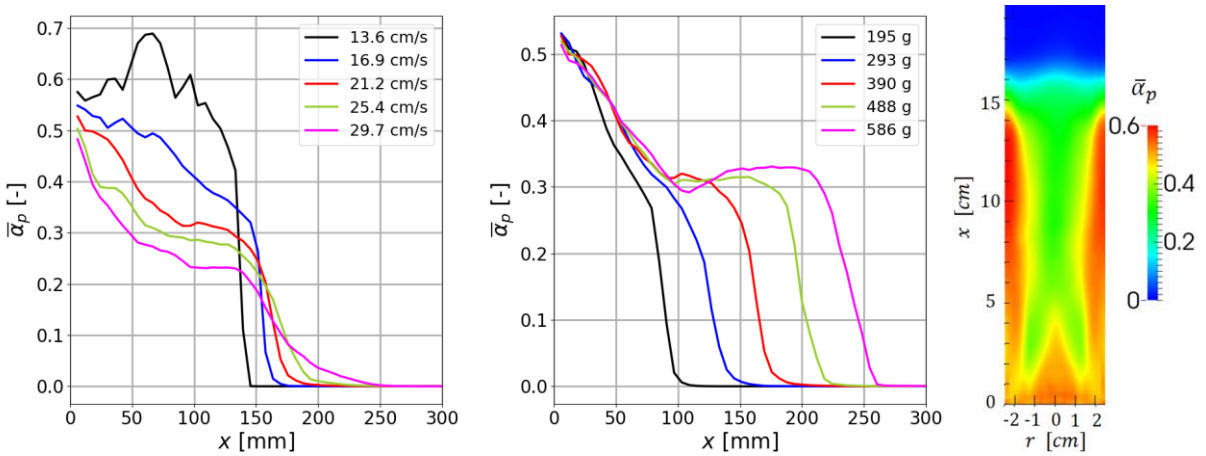


**Figure 5:** Profiles of time-averaged particle volume fraction along the centerline axis at varied superficial gas velocity (left) and sand mass (right).

- **Simulations of up-scaled fluidized bed**

In order to study the effect of up-scaling on the operational behavior of the considered fluidized bed, an approach applying a constant pressure drop and bed height has been chosen. This has been achieved by using a constant superficial gas velocity and particle size distribution for different up-scaled fluidized beds. In this way, the bed inventory yields a quadratic increase with the reactor diameter $d_R$ ($m_S \propto d_R^2$), whereas the bubbling fluidization regime remains unchanged. In the current case, $d_R$ has been varied at 3, 5 and 10 cm. For the numerical simulation, the grid resolution in the radial direction with 1 mm is kept constant for all up-scaled reactors, while the grid distribution in axial direction remains the same. This leads to a quadratic increase of the overall number of finite volumes with the reactor diameter, i.e., 48,000 150,000 and 937,500 for the cases with $d_R$ = 3, 5 and 10 cm. The number of tracked Lagrange

parcels increases while up-scaling the reactor due to increased mass of sand, which is set to 1.2, 4.0 and 12 million with increased $d_R$ at 3, 5 and 10 cm.

The left-hand side of Fig.6 depicts instantaneous contours of $\varepsilon$ on a meridian plane across the centerline axis for different reactor sizes, along with the sand particles indicated by the black points. The morphological structure of the fluidized bed is dominated by large bubbles rising along the centerline axis for the smallest reactor with $d_R$ = 3 cm, where the size of the bubbles is almost equal to the diameter of the tube in this case. This is attributed to the narrow domain bounded by the reactor wall, so that there is only a very limited pathway for the bubbles to pass through, leading to a fast coalescence of the small bubbles. In this case, the sand particles are driven by the large bubbles to the upper side of the fluidized bed, without being recirculated to the vicinity of the wall. At increased reactor size with $d_R$ = 5 cm, there is more space between the dominating large bubbles and the reactor wall, which allows formation of a low-speed region close to the wall and a recirculation of the sand particles there. By further increasing the reactor size to $d_R$ = 10 cm, the number of bubbles is increased significantly due to the increased gas mass flow rate, where two arrays of rising bubbles are generated without coalescing with each other to form larger bubbles. In addition, the sand particles accumulate and fall down not only in the near-wall regions, but also along the symmetry axis. In this case, the gas flow recirculates towards the centerline axis due to the expansion of the flow domain, which drives the sand particles to the centerline axis.

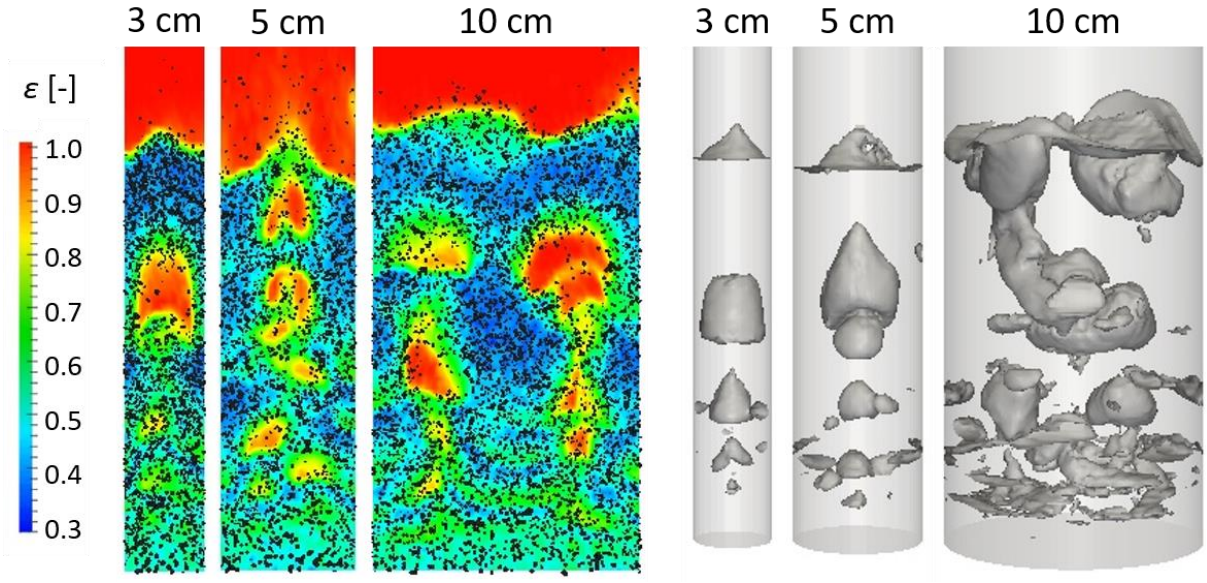


**Figure 6:** Instantaneous contours (left) and iso-surfaces (right) of void fraction for up-scaled fluidized bed reactors with a diameter of $d_R$ = 3, 5 and 10 cm.

Figure 6 on the right shows line-of-sight views of snapshots of $\varepsilon$ = 0.66 iso-contours, which illustrate 3D structures of the bubbles for different cases. It can be detected, that the distance between the bubbles and the wall increases with $d_R$. The hydrodynamics of the fluidized bed is dominated by large-scale bubbles with sizes close to the reactor diameter for the cases with a relatively small $d_R$ at 3 cm and 5 cm, whereas the bubbles rise along multiple off-centered columns in the case of $d_R$ = 10 cm.

The same behavior can be detected from Fig.7 on the left, showing the time-mean contours of $\varepsilon$ on the meridian cutting plane across the symmetry axis. For $d_R$ = 3 cm and 5 cm, $\bar{\varepsilon}$ is largest along the centerline axis due to the large-scale bubbles, which dominate the whole reactor. On the contrary, $\bar{\varepsilon}$ is low at the symmetric axis in the case of $d_R$ = 10 cm, which indicates an accumulation of sand particles there. This is attributed to the rising bubbles along two off-centered axes, resulting in an additional recirculation of the gas flow towards the centerline axis. Figure 7 on the right shows axial profiles of the time-mean volume fraction of sand particles $\bar{\alpha}_P$, which reveals an increase of the particle concentration with increased reactor dimension along the centerline axis. This is caused by an increased momentum transfer from the gas to the solid phase in the lateral direction while increasing $d_R$. Therefore, use of up-scaled reactors is more beneficial concerning a more efficient mixing of the bed materials and elimination of wall effects.

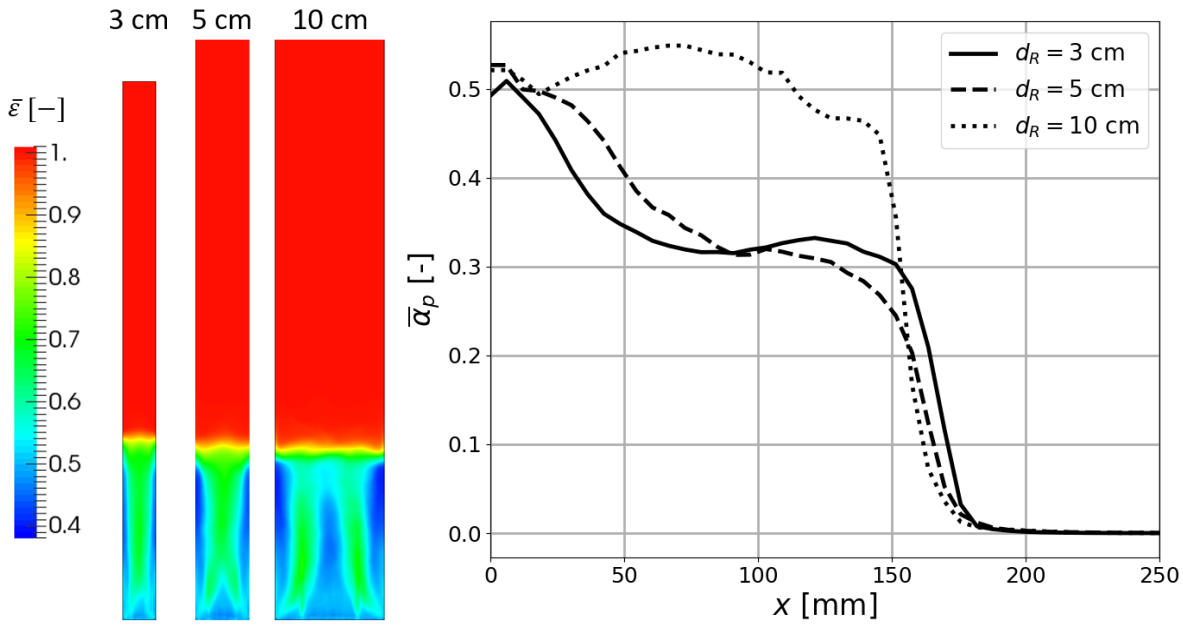


**Figure 7:** Time-mean contours of porosity on a cutting plane through the centerline axis (left) and profiles of time-averaged solid volume fraction along the symmetry axis for up-scaled fluidized bed reactors with a diameter of $d_R$ = 3, 5 and 10 cm.

## Conclusion

Numerical simulations have been carried out in order to gain detailed knowledge regarding the hydrodynamic behavior of a laboratory-scale fluidized bed reactor, which was designed for fundamental study of plastic pyrolysis. Objective of the work is to establish a suitable numerical setup and to validate the multiphase Euler-Lagrange MP-PIC approach, which can be further used for simulation of plastic pyrolysis in fluidized beds. The achieved results are summarized below:

- A numerical setup for 3D, transient simulation of dense particle-gas flow in fluidized beds has been generated in the framework of OpenFOAM.
- The morphological behavior concerning fluidization regime has been reproduced well by the numerical simulations.
- The calculated pressure drop $\Delta p$ agrees well with measured data, which shows a quasi-linear increase with the bed inventory $m_S$ and is almost constant at varied superficial gas velocity $u_G$.
- By up-scaling the reactor at constant $\Delta p$ and $u_G$, the bubbling fluidization regime remains unchanged. However, the number of formed bubbles is increased significantly for up-scaled reactor. In particular, bubbles along multiple columns or off-centered axes are detected for the largest fluidized bed, whereas large-scale bubbles with a similar size of the reactor diameter rising along the centerline axis dominate the hydrodynamics of the smaller reactors.

The simulations provide an insight into the hydrodynamic behavior of the fluidized bed and confirm strong correlations of the characteristic behavior with the general operating parameters. In addition, the good agreement between experiments and simulations validates the computational setup and numerical approach used in this work, so that these can be used for an in-depth analysis considering the plastic particles as well as their interactions with sand beds in terms of momentum and heat exchange.

## Acknowledgments

The authors gratefully acknowledge the financial support by the Helmholtz Association of German Research Centers (HGF), within the research program MTET (Materials and Technologies for the Energy Transition). This work utilized computing resources provided by the High Performance Computing Center Stuttgart (HLRS) at the University of Stuttgart and the Steinbuch Centre for Computing (SCC) at the Karlsruhe Institute of Technology.

## References


[1] Harrison R. M., Hester R. E.: *Plastics and the Environment*, The Royal Society of Chemistry, London, ISBN: 978-1-78801-241-6, 2018

[2] Plastics Europe: *Plastics - the Facts 2022*, https://plasticseurope.org/knowledge-hub/plastics-the-facts-2022/, 2022

[3] Geyer R., Jambeck J.R., Law K.L.: *Production, use, and fate of all plastics ever made*, Sci. Adv., 3, e1700782, 2017.

[4] Hundertmark T., Mayer M., McNally C., Simons T.J., Witte C.: *How plastics waste recycling could transform the chemical industry*, McKinsey & Company, 2018

[5] Schyns Z.O.G., Shaver M.P.: *Mechanical recycling of packaging plastics: A review*, Macromolecular rapid communications, 42, 3, 2000415, 2021.

[6] Dogu O., Pelucchi M., Van de Vijver R., Van Steenberge P.H.M., D'hooge D.R., Cuoci A., Mehl M., Frassoldati A., Faravelli T., Van Geem K.M.*: The chemistry of chemical recycling of solid plastic waste via pyrolysis and gasification: State-of-the-art, challenges, and future directions*, Progress in Energy and Combustion Science, 84, 100901, 2021.

[7] Artetxe M., Lopez G., Amutio M., Elordi G., Bilbao J., Olazar M.: *Cracking of high density polyethylene pyrolysis waxes on HZSM-5 catalysts of different acidity*, Industrial & Engineering Chemistry Research, 52, 31, 10637-10645, 2013.

[8] Mastral F.J., Esperanza E., Berrueco C., Juste M., Ceamanos J.: *Fluidized bed thermal degradation products of HDPE in an inert atmosphere and in air–nitrogen mixtures*, Journal of Analytical and Applied Pyrolysis, 70, 1, 1-17, 2003.

[9] Vollmer I., Jenks M.J.F., Roelands M.C.P., White R.J., van Harmelen T., de Wild P., van der Laan G.P., Meirer F., Keurentjes J.T.F., Weckhuysen B.M.: *Beyond Mechanical Recycling: Giving New Life to Plastic Waste*, Angew Chem Int Ed Engl, 59, 36,15402-15423, 2020.

[10] Soni V.K., Singh G., Vijayan B.K., Chopra A., Kapur G.S., Ramakumar S.S.V.: *Thermochemical recycling of waste plastics by pyrolysis: a review*, Energy & Fuels, 35, 16, 12763-12808, 2021.

[11] Kaminsky W., Menzel J., Sinn H.: *Recycling of plastics*, Conservation & Recycling, 1, 1, 91-110, 1976.

[12] Kaminsky W.: *Pyrolysis of plastic waste and scrap tyres in a fluid bed reactor*, Resource recovery and conservation, 5, 3, 205-216, 1980.

[13] Cheng Z., Tan Z., Guo Z., Yang J., Wang Q.: *Technologies and fundamentals of waste heat recovery from high-temperature solid granular materials*, Applied Thermal Engineering, 179, 115703, 2020.

[14] Ma J., Wang J., Tian X., Zhao H.: *In-situ gasification chemical looping combustion of plastic waste in a semi-continuously operated fluidized bed reactor*, Proceedings of the Combustion Institute, 37, 4, 4389-4397, 2019.

[15] Kuerten J.G.M.*: Point-Particle DNS and LES of Particle-Laden Turbulent flow - a state-of-the-art review*, Flow Turbulence Combust, 97, 689–713, 2016.

[16] Snider D.M., O`Rourke P.J., Andrews M.J.: *An incompressible two-dimensional multiphase particle-in-cell model for dense particle flows*, United States: N. p., 1997.

[17] Alobaid F., Almohammed N., Farid M.M., May J., Rößger P., Richter A., Epple B.: *Progress in CFD Simulations of Fluidized Beds for Chemical and Energy Process Engineering*, Progress in Energy and Combustion Science, 91, 100930, 2022.

[18] Snider D.M.: *An Incompressible Three-Dimensional Multiphase Particle-in-Cell Model for Dense Particle Flows*, Journal of Computational Physics, 170, 2, 523-549, 2001.

[19] O'Rourke P.J., Snider D. M.: *Inclusion of collisional return-to-isotropy in the MP-PIC method, Chemical Engineering Science*, 80, 39-54, 2012.

[20] OpenFOAM: *ESI OpenCFD Release OpenFOAM v2112*, https://www.openfoam.com/news/main-news/openfoam-v2112, 2021.

[21] Michaelides E.E., Crowe C.T., Schwarzkopf J.D.: *Multiphase Flow Handbook*, CRC Press, Boca Raton, ISBN: 978-1498701006, 2016